Ceramics International xxx (xxxx) xxx

Contents lists available at ScienceDirect

Ceramics International

journal homepage: www.elsevier.com/locate/ceramint

Effect of magnetron sputtering Ti-doped NbN coating on corrosion and scaling behavior of H62 brass

Wei Li *, Can Xiong, Xiulan Li, Xinjun Zhou, Yao Chen, Fei You, Zhengyu Guo, Yuan Zhang, Gui He

Faculty of Mechanical Engineering, Sichuan University of Science & Engineering, Yibin, 644000, China

ARTICLE INFO

Keywords:
Magnetron sputtering
Ti doping
NbN coating
H62 brass
Corrosion
Scaling

ABSTRACT

Copper and its alloys possess excellent properties, making them widely used in various fields such as marine engineering, chemical processing, and energy production. However, in certain environments characterized by metal cation and elevated salt concentrations, these alloys may experience corrosion and scaling, which can reduce their lifespan and limit their applications. In this study, NbTiN composite coatings with varying titanium target powers were prepared on the surface of H62 brass using radio frequency (RF) and direct current (DC) magnetron co-sputtering techniques. The microstructure, chemical composition, corrosion resistance, wettability, and scaling behavior of the NbTiN coating in a saturated $CaCO_3$ solution were systematically investigated. The results indicated that doping with Ti inhibits the growth of the columnar crystal structure in the coating, enhancing the surface uniformity and density. However, when the Ti target power is excessively high, it tends to promote the formation of columnar crystals and surface defects. The NbTiN coating exhibits optimal corrosion resistance at a Ti target power of 110 W, with a corrosion current density of 1.148×10^{-7} A/cm^2, two orders of magnitude lower than that of the bare brass sample (1.244×10^{-5} A/cm^2). Additionally, the maximum water contact angle of the coating was approximately 98.8° ± 1.4°, indicating hydrophobic properties. Fouling tests demonstrated that the amount of fouling on the NbTiN coating samples initially decreased and then increased with higher Ti target power. At a Ti target power of 110 W, the fouling of the coated samples reached a minimum of 0.0387 mg/cm^2, achieving a scale inhibition rate of 77.94 %. This research provides a novel approach to developing antifouling and corrosion-resistant coatings for copper alloys through careful composition design, structural optimization, and functional integration. This work is significant for advancing the development and application of metal surface engineering.

1. Introduction

In the course of industrial civilization, metallic materials have often emerged as the core carriers of engineering equipment. Among these, copper and its alloys are widely used across various fields, including marine engineering, the energy and chemical industries, aerospace, and electronics. This extensive adoption is primarily due to their excellent thermal and electrical conductivity and ductility [1–4]. However, under real-world service conditions, copper alloys exhibit significant vulnerabilities. Their intrinsic hydrophilic properties make them susceptible to accelerated corrosion, dirt accumulation, microbial adhesion and frosting when exposed to complex environments characterized by ions such as Cl^-, Ca^{2+}, H^+, as well as low temperatures [5]. Take the power transmission system as an example, copper conductors operating in low-temperature, high-humidity environments are particularly prone to the formation of frost corrosion layers, which can degrade electrical conductivity and mechanical strength, thereby threatening the safety of power grids. Similarly, brass heat exchanger tubes operating in chlorine-containing media face substantial risks, including pitting. In such environments, dissolved ions such as Ca^{2+} and Mg^{2+} can react with acid root ions, contributing to the formation of dense scale layers on the surfaces of the heat exchanger tubes, resulting in a reduction in the heat transfer coefficient of the heat exchangers and an increase in heat transfer resistance. The strong polarity of copper alloy surfaces facilitates the adsorption of water molecules, amplifying their hydrophilicity. These characteristics not only enhance the reactivity of the metal interface but also provide an ideal “nest” for the adhesion of corrosion products, scale, and microbial colonization. Collectively, these factors

* Corresponding author.
E-mail address: liweibuqi@163.com (W. Li).

https://doi.org/10.1016/j.ceramint.2025.11.424
Received 28 August 2025; Received in revised form 7 November 2025; Accepted 28 November 2025
Available online 28 November 2025

reduce the efficiency of engineering equipment, heightened risk of equipment damage, energy losses, and increased production costs [6–8]. In addition, there are higher costs for equipment maintenance and cleaning. Corrosion and scaling have been reported to cost the U.S. industrial sector approximately $10 billion per year [9]. Therefore, it is essential to prioritize surface modification of copper alloys. The key goals include enhancing surface energy, reducing the reactivity of corrosive ions with the alloy matrix, and improving overall chemical stability. This not only holds significant economic potential but also carries profound implications for the industrial application of copper alloys.

Surface modification technology serves as a feasible approach to enhance the wear resistance, corrosion resistance, and interfacial activity of metallic materials [10]. Currently, common surface modification methods encompass magnetron sputtering [11–14], chemical vapor deposition [15,16], and electroplating [17]. Among these methods, magnetron sputtering is characterized by the sputtering and deposition of target atoms onto a substrate surface, accomplished through the bombardment of the target with plasma facilitated by an electromagnetic field [18]. This method offers precise control over the composition, thickness, and morphology of the resultant coating. Notably, it imposes no constraints on the type of substrate, ensuring strong film adhesion, uniform distribution, high sputtering efficiency, and the elimination of waste liquid or gas generation. Studies have shown that magnetron sputtering technology has vast application prospects in the field of antifouling and corrosion resistance of metal surfaces [19]. For instance, Oon et al. [20] employed RF magnetron sputtering to apply titanium coatings on the surface of a heat exchanger, subsequently examining the deposition of calcium carbonate on both the titanium-coated surface and the substrate. Their findings demonstrated that titanium-coated specimens exhibited significantly reduced fouling deposits and enhanced corrosion resistance, ultimately prolonging the efficiency and service life of the heat exchanger. Similarly, Shaikh et al. [21] deposited a layer of zirconium on the surface of a heat exchanger test section using radio frequency magnetron sputtering and investigated its effect on the accumulation and mitigation of $CaCO_3$ fouling. The results indicated that zirconium-coated surfaces displayed hydrophobicity with reduced $CaCO_3$ deposition, achieving a contact angle of 105°. Furthermore, Meng et al. [22] prepared non-precious metal coatings of Ta, Nb, and Ti using the magnetron sputtering method, and investigated the effect of different coatings on the corrosion resistance of uncoated titanium substrates. The results showed that the Nb coating had the lowest corrosion current density, which decreased from 9.57 μA/cm^2 to 0.02 μA/cm^2.

Compared with monolithic metals, metal nitrides exhibit a distinctive hybrid structure characterized by the coexistence of metallic and covalent bonding. This structural feature not only confers excellent chemical stability but also provide lower surface energy, which further enhances the hydrophobicity of the corresponding coatings [23]. Among various metal nitrides, niobium nitride (NbN) has emerged as an ideal choice for surface modification due to its outstanding wear resistance, corrosion resistance, and electrical conductivity [24]. The incorporation of NbN can significantly enhance the overall performance of metals concerning wear resistance, corrosion resistance, and hydrophobicity [25]. However, the application of single metal nitride coatings in harsh environments often leads to the formation of surface defects, such as holes and cracks, which provide pathways for corrosive media and may result in localized corrosion or even delamination of the coating. To address this issue, researchers have developed multi-component coatings by doping additional elements, thus creating a structure that effectively mitigates defect formation and modifies the chemical bonding state [26,27]. This approach enhances the performance of the coatings, allowing them to withstand increasingly complex and dynamic service environments [28,29]. For instance, Ren et al. [30] fabricated a Nb-Y-N coating using magnetron sputtering and explored the influence of varying Y content on the properties of NbN coatings. Their findings indicate that the hardness of the Nb-Y-N coating increased to 25.1 GPa, which is 1.5 times higher than that of pure NbN, when the percentage of Y atomic content is 4.6 %. The introduction of Y also affected the wetting states of the surface, exhibiting hydrophobicity with a maximum water contact angle of 116°. Hao et al. [31] prepared Ce-doped NbN coatings, demonstrating that even a small amount of Ce doping could enhance the hardness, wear resistance, and hydrophobicity of the coatings. Additionally, Ren et al. [32] prepared Ag-doped NbN coatings using magnetron sputtering techniques, which showed hydrophobic properties, with an increase in hardness from 17.27 GPa to 22.44 GPa upon the inclusion of 6.2 % Ag atoms, resulting in a maximal water contact angle (WCA) of 118°.

Doping elements (such as Al and Si) into niobium nitride coatings can not only alter the coating's growth structure and reduce defect density, but also lead to the formation of new phases, thereby enhancing properties such as hardness, wear resistance, and thermal stability [33,34]. However, insufficient attention has been paid to the corrosion resistance, hydrophobicity, and anti-fouling properties of element-doped niobium nitride coatings. In addition, systematic studies involving Ti-doped NbN coatings remain relatively scarce, and the mechanisms by which Ti doping affects the microstructure, physical phases, and properties of these coatings are not well understood. Therefore, this study selects Ti, renowned for its excellent corrosion resistance, mechanical strength, and low density, as the doping element. We employed RF and DC co-sputtering within a magnetron sputtering system to fabricate NbN coatings doped with varying Ti target powers on the surface of H62 brass. The microstructures and tissue compositions of NbTiN coating surfaces were systematically explored, along with an examination of how Ti doping influences the scaling and corrosion behaviors of the NbTiN coating samples in a $CaCO_3$ environment. This research aims to provide valuable insights for the selection and optimization of antifouling and corrosion-resistant coatings for copper surfaces.

2. Experimental procedures

2.1. Coating preparation

The substrates used in this study consisted of commercial H62 brass plates and monocrystalline silicon wafers (001), the latter being used for the observation of coating cross-sectional morphology. The chemical composition of the brass matrix is characterized by a Zn content ranging from 36 wt% to 38 wt%, with Cu constituting the remainder. The brass plates were cut into specimens measuring 15 mm × 15 mm × 2 mm using electrical discharge machining (EDM) (DK77C, Jiangsu Sanxing Machinery Manufacturing Co., Ltd., China). The surfaces of the specimens were sequentially ground with metallographic sandpapers of grits 400#, 800#, 1000#, 1500#, and 2000#, followed by polishing with a 0.5 μm diamond paste. Following polishing, the specimens were subjected to ultrasonic cleaning with acetone, anhydrous ethanol, and deionized water for 15 min, subsequently dried in a drying oven, and stored in a sealed container for future use. All solvents utilized during the experiments were deionized water, and all reagents were of analytical purity grade.

Various Ti-doped NbN coatings were deposited on copper sheets using a magnetron sputtering coater (JCP-500, Techno Technology Co., Ltd., China). The sputtering targets included a metal Nb target (purity of 99.95 %, dimensions of φ50.8 × 4 mm) and a metal Ti target (purity of 99.999 %, dimensions of φ76.2 × 4 mm). The Nb target was powered by a direct current (DC) power supply, while the Ti target was energized by a radio frequency (RF) power supply. The discharge gas mixture employed during the sputter coating process consisted of Ar (purity of 99.999 %) and N_2 (purity of 99.999 %). Prior to deposition, the pretreated specimens underwent cleaning with anhydrous ethanol. Subsequently, the specimens were placed in a chamber after being nitrogen blow-dried. The distance between the target and the substrate was adjusted to 120 mm, with the target tilted at a 45° angle relative to the

substrate normal. The vacuum of the chamber was established at 3 × 10^{-3} Pa using a turbo molecular pump. Glow cleaning of the substrate was conducted for 10 min to remove surface impurities, accomplished by adjusting the argon flow rate to 50 sccm under a bias voltage of −800 V. Before introducing nitrogen into the sputtering system, a 30 min deposition of niobium was performed as a binding layer to ensure the adhesion of the coating to the substrate. The sputtering current for the Nb target was maintained at 0.25 A, the bias voltage was kept constant at −100 V, and the argon (Ar) flow rate was set to 25 sccm. The deposition of NbTiN coatings was performed through DC combined with RF co-sputtering, with flow rates of 20 sccm for argon (Ar) and 5 sccm for nitrogen (N_2), maintaining a working pressure of 0.8 Pa. The quantity of Ti doping was precisely controlled by varying the power supplied to the RF Ti target within the range of 70 W–130 W in 20 W increments, and complete over a period of 60 min. The specific steps in the coating preparation process and corresponding deposition parameters are detailed in Fig. 1 and Table 1.

2.2. Coating characterization

The micro-morphological and structural features of the sample surfaces and cross-sections were investigated using field emission scanning electron microscopy (FESEM, CIQTEK Co-SEM5000, China) at an accelerating voltage of 10 kV. To analyze the surface chemical bonding states of the samples, X-ray photoelectron spectroscopy (XPS, ESCALAB 250Xi, Thermo Fisher Scientific, USA) was employed, utilizing monochromatic Al-K_α radiation as the X-ray light source at an energy of 1486.68 eV. The anode was operated at a power setting of 96 W (12 kV, 8 mA), with a spot area of 2 mm^2, while maintaining a system pressure of less than 1 × 10^{-9} mbar. Prior to spectral analysis, ion beam etching was performed with an Ar^+ ion beam at an energy of 3000 eV and an incidence angle of 45° for a duration of 5 min to eliminate surface contaminants.

2.3. Electrochemistry test

The electrochemical corrosion performance of the specimens was assessed in a 3.5 wt% NaCl solution using an electrochemical corrosion friction and wear tester (Huahui Instrument, MFT-EC4000, Huahui Instrument Technology Co., Ltd., China) from Huahui. The corrosion potential and corrosion current of both the substrate and coating were determined through Tafel polarization curve extrapolation. Additionally, the alternating current impedance (EIS) of the coating surface was tested to further verify its corrosion resistance. A standard three-electrode system was used, comprising the sample as the working electrode, a platinum electrode as the auxiliary electrode, and Ag/AgCl as the reference electrode, with the exposed working area of the sample being 1 cm^2. The corrosion medium was a 3.5 wt% NaCl solution, and the test was conducted under normal temperature conditions. Prior to electrochemical measurements, an open-circuit potential (OCP) test was performed for 30 min to ensure system stabilization. Following this, EIS was conducted over a frequency range of 10^{-2} Hz–10^5 Hz with an amplitude of 10 mV. Dynamic potential polarization (IE) was evaluated across a voltage range of −0.6 V–1.0 V with a scan rate of 1 mV/s. The electrochemical impedance data were subsequently fitted using Zsimp-Win software, allowing for a parametric analysis of the corrosion resistance characteristics of the specimens using the equivalent circuit and its components. All samples underwent consistent electrochemical testing parameters, with each sample group subjected to three parallel replicate tests.

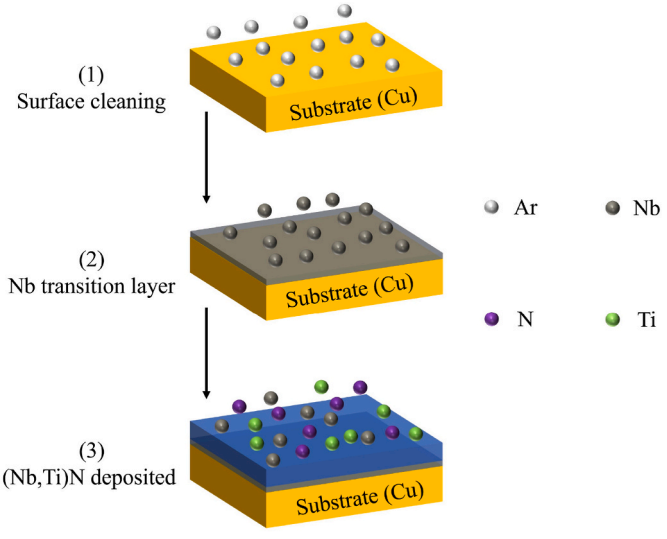

Fig. 1. Flow chart of coating preparation: (1) Surface cleaning, (2) Nb transition layer, and (3) (Nb,Ti)N deposited.

Table 1
Process parameters for magnetron sputtering deposition of coatings.

Step	Bias voltage (V)	RF power (W)	DC current (A)	Time (min)	Air flow (sccm)	N_2 flow (sccm)
1	−800	–	–	10	50	–
2	−100	–	0.25	30	25	–
3	−100	0/70/90/110/130	0.25	60	20	5

2.4. Water contact angle measurements

A contact angle meter (JY-PHb, China) was used to measure the static water contact angle (θ) of the samples at room temperature, and the size of the static water contact angle was used to characterize the wetting behavior of the coating surface. A 2 μm diameter micropipette was used to control the volume of deionized water droplets, with the contact angle being recorded after the droplets had stabilized on the specimen surface. Five different positions of the same specimen were selected for measurements, and the average contact angle was computed from these data, with a liquid volume of 3 μL.

2.5. Formation of $CaCO_3$ scale on different surfaces of the brass

In accordance with the methodology detailed in the literature [35], sodium bicarbonate ($NaHCO_3$) and anhydrous calcium chloride ($CaCl_2$) were used as raw materials to generate a supersaturated $CaCO_3$ solution, characterized by a high concentration of 360 mg/dm^3 Ca^{2+} and 1140 mg/dm^3 HCO_3^- as the scaling solution. The chemical reaction involved in the formation of $CaCO_3$ is expressed by equation (1) [[36]]:

$$2NaHCO_3 + CaCl_2 \rightarrow CaCO_3 + 2NaCl + H_2O + CO_2 \quad (1)$$

The mechanism by which the Ti-doped NbN coating influences the rate of $CaCO_3$ adsorption crystallization was evaluated through a weighing method. To minimize the effect of the gravity error of dirt, the specimens were vertically suspended in a water bath heated to 60 °C for a duration of 12 h, with removals occurring every 3 h for natural drying at room temperature. The samples were weighed, and the mass of dirt deposited per unit surface area was calculated using equation (2) [36]:

$$W_s = (W_1\text{-}W_0) / A \quad (2)$$

Where W_1 and W_0 are the mass of the sample before and after the scaling test, respectively, and A denotes the surface area of the sample. All the tested samples were subjected to three repeated experiments, and the average value was computed from these data, with taken to ensure statistical reliability.

3. Results and discussion

3.1. Coating morphology and composition

Fig. 2 illustrates the surface microscopic morphology of the NbTiN coating at varying Ti target powers. Analyzing the surface morphology (Fig. 2(a)–(e)), it is evident that the surface of the NbN (0 W) coating exhibits a clustered spherical structure with small aggregated particles. This phenomenon results from the crystallization of the film following irregular grain growth during the sputtering process. However, the surface of the undoped coating is characterized by roughness and includes several defects, such as pits and holes, which may facilitate the diffusion of corrosive mediators and ultimately degrade the electrochemical properties of the coating [37,38]. It is noteworthy that with the introduction of Ti elements, a reduction in the number of defects is observed, and with an increase in Ti target power, the surface of the NbTiN coating gradually demonstrates a denser structure. In particular, when the Ti target power was set to 110 W, the coating surface achieves the highest density and uniformity, with fewer defects compared to other samples. However, when the Ti target power exceeds 110 W, the emergence of craters and cracks on the coating surface occurs, leading to a decline in the surface flatness, which adversely affects the performance of the coating [39]. This observation suggests that Ti doping effectively improves the densification of the coating surface morphology, but excessively high Ti target powers increase the stress during the sputtering process, resulting in the rupture of sparse sections and the formation of surface defects [40–43].

Fig. 3 shows the cross-sectional morphology of the NbTiN coatings doped with varying Ti target powers. From the cross-sectional views (Fig. 3(a)–(e)), it is evident that each coating specimen is well bonded to the substrate, exhibiting no obvious defects and a uniform distribution. Among these, the undoped NbN coating has a minimum thickness of approximately 544 nm and displays a typical columnar crystal structure. This phenomenon can be attributed to the magnetron sputtering deposition process, where sputtered Nb atoms have poor diffusion abilities and do not fully disperse across the substrate surface. During the sputtering process, the crystal nuclei grow predominantly perpendicular to the substrate. Consequently, post-sputtering atoms are rapidly deposited onto the pre-existing atoms, leading to the formation of a columnar crystal structure [44]. Notably, no significant interfacial delamination was observed between the Nb binding layer and the NbN coating. This can be explained by the similarity in crystal growth processes between Nb metals and NbN coatings, allowing for continuous and unhindered growth of columnar crystals along the Nb and NbN layers, resulting in a less distinct coating interface (Fig. 3(a)). As the Ti target power increases, the thickness of the NbTiN layer gradually increases from 262 nm to 314 nm, with noticeable delamination occurring. This delamination is primarily due to Ti doping, which alters the coating deposition process and modifies the chemical composition, resulting in an interrupted columnar crystal structure at the coating interface. This results in a clear boundary between the Nb and NbTiN layers (Fig. 3(b)–(e)). Interestingly, Ti doping promotes the formation of dense layers, which helps reduce defects such as micropores and cracks [45,46]. When the Ti target power is set at 110 W, the inhibitory effect on the columnar crystal structure is minimized, and the coating thickness reaches approximately 561 nm. However, further increasing the power beyond 110 W results in a significant increase in the thickness from 561 nm to 578 nm. Excessive Ti doping leads to a considerable thickening of the

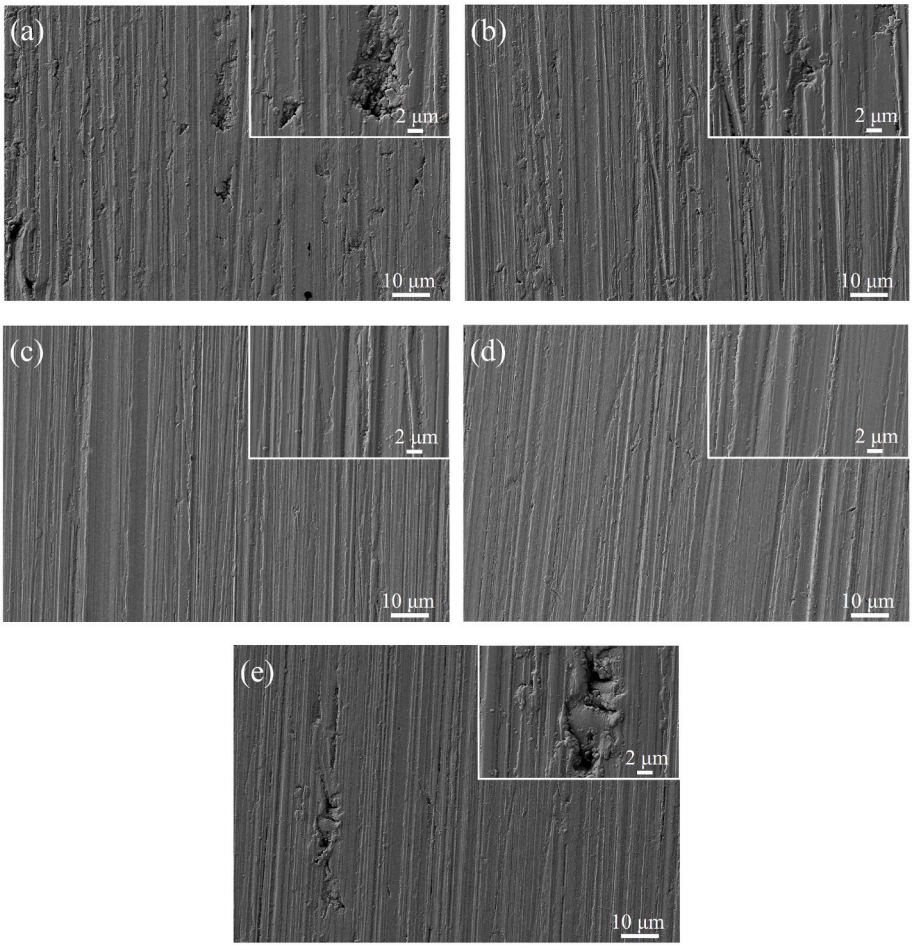

Fig. 2. The surface morphology of NbTiN coatings prepared with different Ti target powers: (a) 0 W, (b) 70 W, (c) 90 W, (d) 110 W, and (e) 130 W.

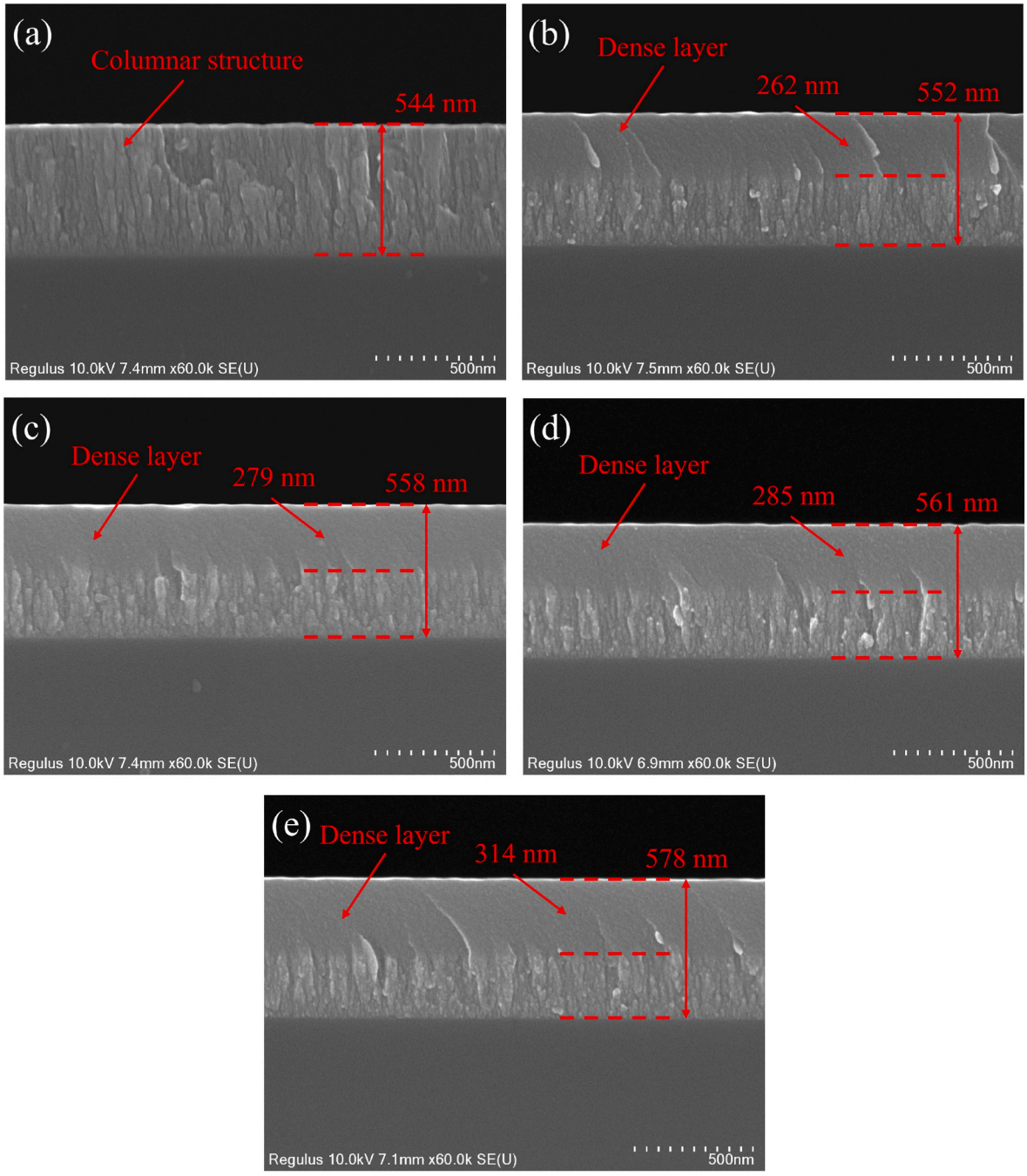

Fig. 3. The cross-sectional morphology of the NbTiN coating at various Ti target powers: (a) 0 W, (b) 70 W, (c) 90 W, (d) 110 W, and (e) 130 W.

coating, further promoting the formation of more columnar crystal structures. Therefore, an appropriate amount of Ti doping is beneficial for enhancing the compactness of the coating, while excessive doping encourages the growth of columnar crystals.

The chemical composition and elemental bonding states of the NbTiN coating surfaces were analyzed using XPS. High-resolution XPS fitted spectra for Nb 3*d*, Ti 2*p*, and N 1*s* were provided though XPSpeak 4.1 software. Fig. 4(a) presents the classic general XPS survey spectrum of the NbN and NbTiN(110W) samples. For the NbTiN coating, characteristic orbital peaks corresponding to Nb 3*d*, Ti 2*p*, O 1*s*, and N 1*s* are clearly detected on its surface. Notably, the observed O 1*s* peak was presumably attributed to the adsorbed oxygen species, which are likely generated when the coating was exposed to ambient air after the sample preparation process. In Fig. 4(b), the Nb 3*d* spectra were fitted to reveal three types of chemical bonds: Nb-O, Nb-N, and Nb-N-O. The most prominent feature is the Nb_2O_5 peak, which has a binding energy of 207.1 eV. This peak indicates the oxidation of unbonded Nb atoms in the coating. The second component appears at a binding energy of 206.2 eV, characteristic of NbN. The peak at 208.2 eV suggests the presence of $NbN_{1-x}O_x$ in the coating, likely due to intermediate products formed during the oxidation of NbN [47]. As the Ti target power increases, the Nb 3*d* peaks shift toward higher binding energies, while the intensity of the NbN peaks gradually decreases, with the proportion of Nb-N bonds falling from 20.4 % to 9.4 %. Conversely, the intensity of the Nb_2O_5 peak increases significantly, and the proportion of Nb-O bonds increases from 60.4 % to 81.1 %. This indicates that the doping of Ti atoms reduces the likelihood of bonding between Nb and N atoms. Additionally, because the Ti has a stronger oxygen affinity, it preferentially adsorbs and reacts

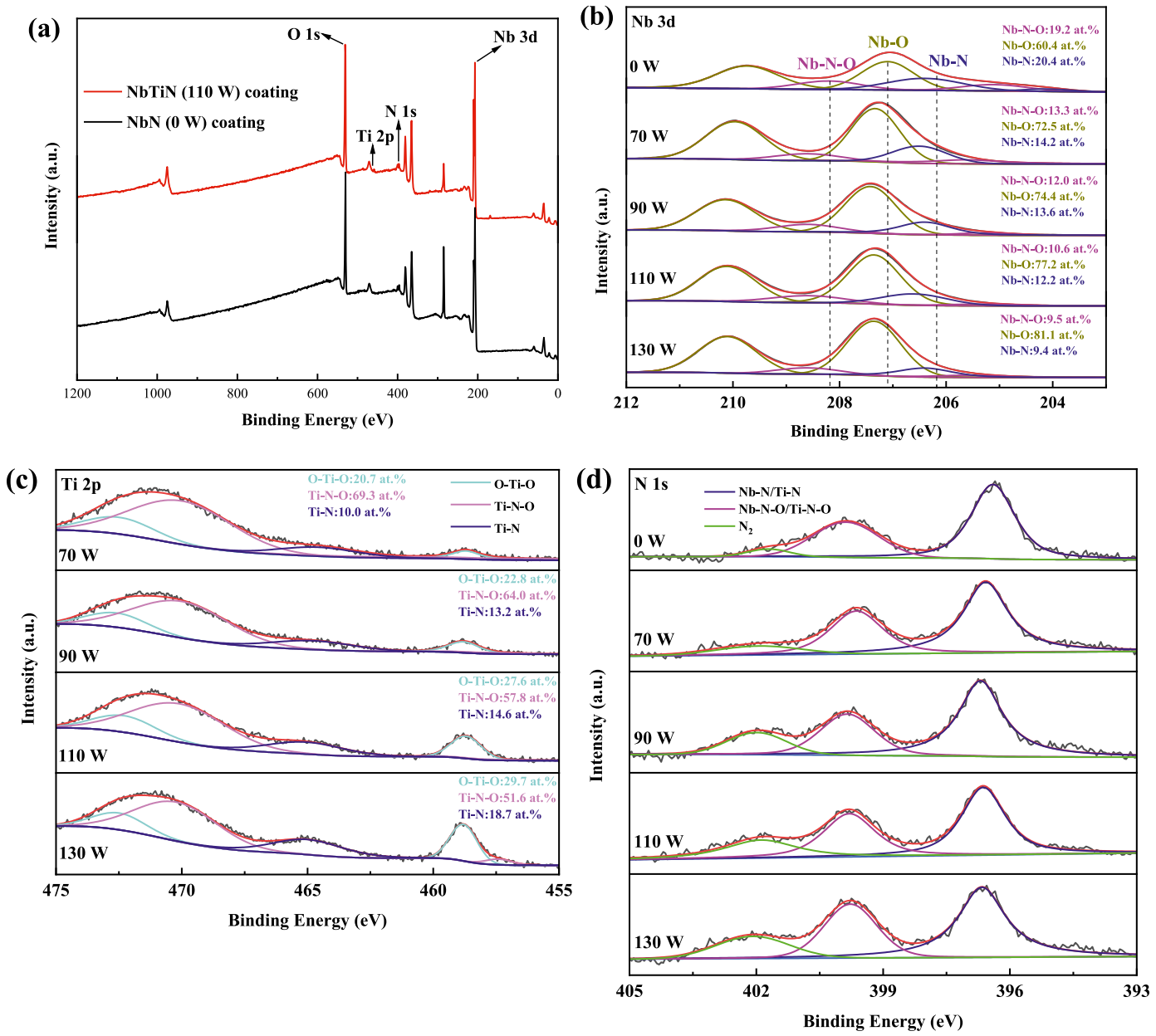

Fig. 4. XPS spectra of NbTiN coatings: (a) General XPS scan of sample (b) Nb 3*d*, (c) Ti 2*p*, and (d) N 1*s*.

with oxygen atoms. This leads to the exposure of active Nb atom sites in the coating, promoting the self-oxidation of Nb atoms on the surface of the NbN coating [48]. Three types of titanium bonding states – TiN_xO_y, TiO_2, and TiN – are detected in the Ti 2*p* spectrum (Fig. 4(c)). Peaks with binding energies of 470 eV and 457.4 eV correspond to TiN_xO_y; peaks at 472.5 eV and 458.6 eV are attributed to TiO_2; and the peak with a binding energy of 464.5 eV aligns with TiN [49,50]. The proportion of Ti-N bonds increases from 10.0 % to 18.7 % as the Ti target power rises from 70 W to 130 W, indicating that higher Ti target power promotes the formation of Ti-N bonds in the NbTiN coating. The N 1*s* spectrum is shown in Fig. 4(d), the N 1s spectrum exhibits three fitted peaks at binding energies of 396.6 eV, 399.6 eV, and 401.9 eV, corresponding to niobium/titanium nitrides (Nb-N/Ti-N), niobium/titanium oxynitrides (Nb-N-O/Ti-N-O), and molecular nitrogen (N_2), respectively [51,52]. It was observed that with increasing Ti content, the nitride concentration in the coating decreased, while the oxynitride concentration increased, while the content proportion of metal oxynitrides remains lower than that of metal nitrides.

3.2. Electrochemical corrosion behavior test

Fig. 5 shows the potentiodynamic polarization curves of the samples in a 3.5 wt% NaCl solution. These curves can be divided into three main regions: the cathodic polarization zone, the anodic polarization zone, and the passivation zone. The corrosion potential (E_{corr}), corrosion current density (i_{corr}), anodic slope (β_a), cathodic slope ($-\beta_c$), chi-squared of anodic slope ($\chi^2(\beta_a)$) and chi-squared of cathodic slope ($\chi^2(-\beta_c)$) from the potentiodynamic polarization curves were calculated using the Tafel extrapolation method, and the results were summarized in Table 2. It can be seen from Fig. 5 that the polarization curve of the bare brass specimen was found to consist of three distinct regions: the cathodic region, anodic region, and passivation region. A pronounced activation peak was observed around 0.2 V, indicating vigorous corrosion reactions on the bare brass. When the potential exceeded 0.25 V, a well-defined passivation region emerged, during which the corrosion current density decreased initially and then gradually stabilized. In contrast, the NbN-coated specimen exhibited a corrosion potential shift from −0.265

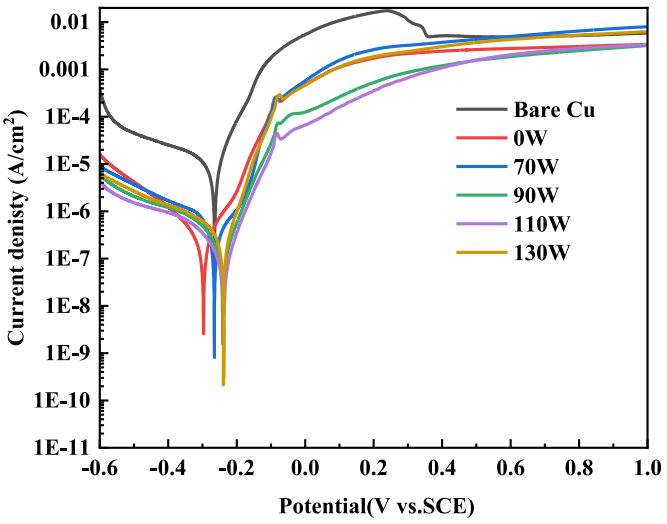

Fig. 5. Dynamic potential polarization curves of different NbTiN coating specimens and bare brass.

V to −0.297 V relative to the bare brass. This negative shift may be attributed to defects in the coating surface (e.g., micropores, cracks), which provide pathways for corrosive media to reach the coating-substrate interface, thereby compromising its chemical inertness. Nevertheless, the corrosion current density of the coated specimen was significantly lower than that of the bare brass, demonstrating that the coating still provides effective protection to the substrate [53,54]. Additionally, as the Ti target power increases, the corrosion potential of the NbTiN coating initially rises and then falls, while the corrosion current density presents a tendency to decrease before increasing again. The corrosion current densities are measured as follows: 3.679×10^{-7} A/cm^2 (0 W), 3.015×10^{-7} A/cm^2 (70 W), 1.857×10^{-7} A/cm^2 (90 W), 1.148×10^{-7} A/cm^2 (110 W), and 2.891×10^{-7} A/cm^2 (130 W), all of which are significantly lower than that of the bare brass substrate (1.244×10^{-5} A/cm^2). Specially, among all the samples, the Nb/(Nb,Ti)N-110 W specimen demonstrates the highest corrosion potential (−0.238 V) and the lowest corrosion current density (1.148×10^{-7} A/cm^2). Compared to the substrate, the corrosion current density is reduced by approximately two orders of magnitude, indicating superior corrosion resistance. This enhanced performance is primarily attributed to the double-layer structure resulting from Ti doping, which effectively blocks the pathway for elongated pinhole defects in the coating. Moreover, at a Ti target power of 110 W, the refinement effect on the columnar crystal structure reaches its optimal state. This not only increases the coating thickness but also significantly diminishes the defect density, thus inhibiting the penetration of corrosive media into the substrate [55]. However, when the Ti target power exceeds 110 W, excessive Ti doping leads to a substantial increase in coating thickness, promoting the formation of columnar crystal structures. Therefore, an appropriate amount of Ti doping can reduce defects in the NbN coating, resulting in improved corrosion resistance and chemical stability. In contrast, excessive Ti doping can create an overly thick coating with increased defects, consequently reducing corrosion resistance.

The corrosion behaviors of both the bare brass substrate and the NbTiN coating were further characterized using electrochemical impedance spectroscopy (EIS), as illustrated in Fig. 6. In Fig. 6(a), all samples exhibit similar capacitive arcs, the radius of which provides a preliminary assessment of corrosion resistance. The coated samples consistently demonstrate larger capacitive arc radii compared to the bare brass. Furthermore, the incorporation of Ti into the NbN coating progressively increases the arc radius with Ti content increasing. However, a notable decrease in radius is observed at a Ti target power of 130 W, indicating reduced corrosion resistance [56]. In contrast, the radii of the capacitive arcs for the NbTiN coating are all larger than those of the brass substrate, indicating an enhancement in corrosion resistance. The capacitive arc pattern of the NbTiN coating is consistent, and as the Ti target power increases, the radius of the capacitive arc first increases and then decreases. Among the samples, the NbTiN coating with a Ti target power of 110 W exhibits the largest capacitive arc radius. This indicates that doping Ti (110 W) into the NbN coating significantly enhances its corrosion resistance, aligning with the results obtained from the polarization curves. The Bode plots in Fig. 6(b) and (c) depict the relationships between frequency, impedance, and phase angle of the NbTiN coating during the corrosion process. Generally, a higher impedance modulus in the low-frequency region indicates better corrosion resistance [57]. As shown in Fig. 6(b), the impedance modulus of the Ti-doped NbN coating is significantly higher in the low-frequency region compared to that of the undoped NbN (0 W) coating, confirming that Ti doping enhances corrosion resistance. In addition, when the Ti target power is at 110 W, its impedance modulus reaches a maximum value of 1.48×10^5 Ω cm^2, showing the best corrosion resistance, consistent with the Nyquist diagram results. Compared to the undoped sample, the Ti-doped NbN coating exhibited a higher and broader phase angle (Fig. 6(c)). At a Ti target power of 130 W, a distinct double-peak structure emerged, corresponding to the presence of two time constants in the phase angle curve. This indicates a dual-layer structural model for the fabricated coating sample, consisting of the surface coating layer and a passive film representing the interface between the substrate and the coating [58].

The equivalent circuit diagrams and respective components are displayed in Fig. 6(d) and (e) were used for a fitting analysis of the corrosion resistance of the bare brass substrate and the NbTiN coating. The fitted data parameters are shown in Table 3. In this context, R_S, R_C, and R_f represent solution resistance, film resistance, and charge transfer resistance, respectively. To account for the dispersion effect of the samples, the constant phase element Q was selected to replace the ideal capacitive reactance in the equivalent circuit model. Additionally, Q_1 and Q_2 represent double-layer capacitance and film capacitance, respectively, while W represents the diffusion element [59,60]. Table 3 indicates that the R_S values for the various samples do not differ significantly, indicating that the tests were carried out under stable conditions. The value of R_f is closely linked to the diffusion resistance of corrosive ions, reflecting the ability to protect metal ions from corrosive dissolution. Compared to the bare brass substrate (R_f value of 8.56×10^2 Ω cm^2), the R_f of the NbN (0 W) coating increases significantly; with the introduction of the Ti element, the R_f of the NbTiN coating improves further. Notably, when the Ti target power is set at 110 W, the R_f of the NbTiN coating exceeds that of the other coating samples, reaching a

Table 2
Fitting parameters for different NbTiN coating specimens and bare brass kinetic potential polarization curves.

Sample	E_{corr} (V vs. SCE)	i_{corr} (A/cm^2)	β_a (V·dec^{-1})	χ^2 (β_a) (V·dec^{-1})	$-\beta_c$ (V·dec^{-1})	χ^2 ($-\beta_c$) (V·dec^{-1})
Bare Cu	−0.265 ± 0.017	(1.244 ± 0.121) × 10^{-5}	0.074 ± 0.013	0.0047	0.423 ± 0.028	0.0058
Nb/(Nb,Ti)N-0W	−0.297 ± 0.013	(3.679 ± 0.432) × 10^{-7}	0.111 ± 0.020	0.0053	0.189 ± 0.015	0.0040
Nb/(Nb,Ti)N-70W	−0.266 ± 0.020	(3.015 ± 0.070) × 10^{-7}	0.099 ± 0.011	0.0014	0.096 ± 0.022	0.0033
Nb/(Nb,Ti)N-90W	−0.241 ± 0.028	(1.857 ± 0.181) × 10^{-7}	0.065 ± 0.016	0.0037	0.158 ± 0.029	0.0022
Nb/(Nb,Ti)N-110W	−0.238 ± 0.010	(1.148 ± 0.220) × 10^{-7}	0.064 ± 0.013	0.0017	0.150 ± 0.009	0.0014
Nb/(Nb,Ti)N-130W	−0.239 ± 0.025	(2.891 ± 0.351) × 10^{-7}	0.056 ± 0.014	0.0029	0.208 ± 0.024	0.0030

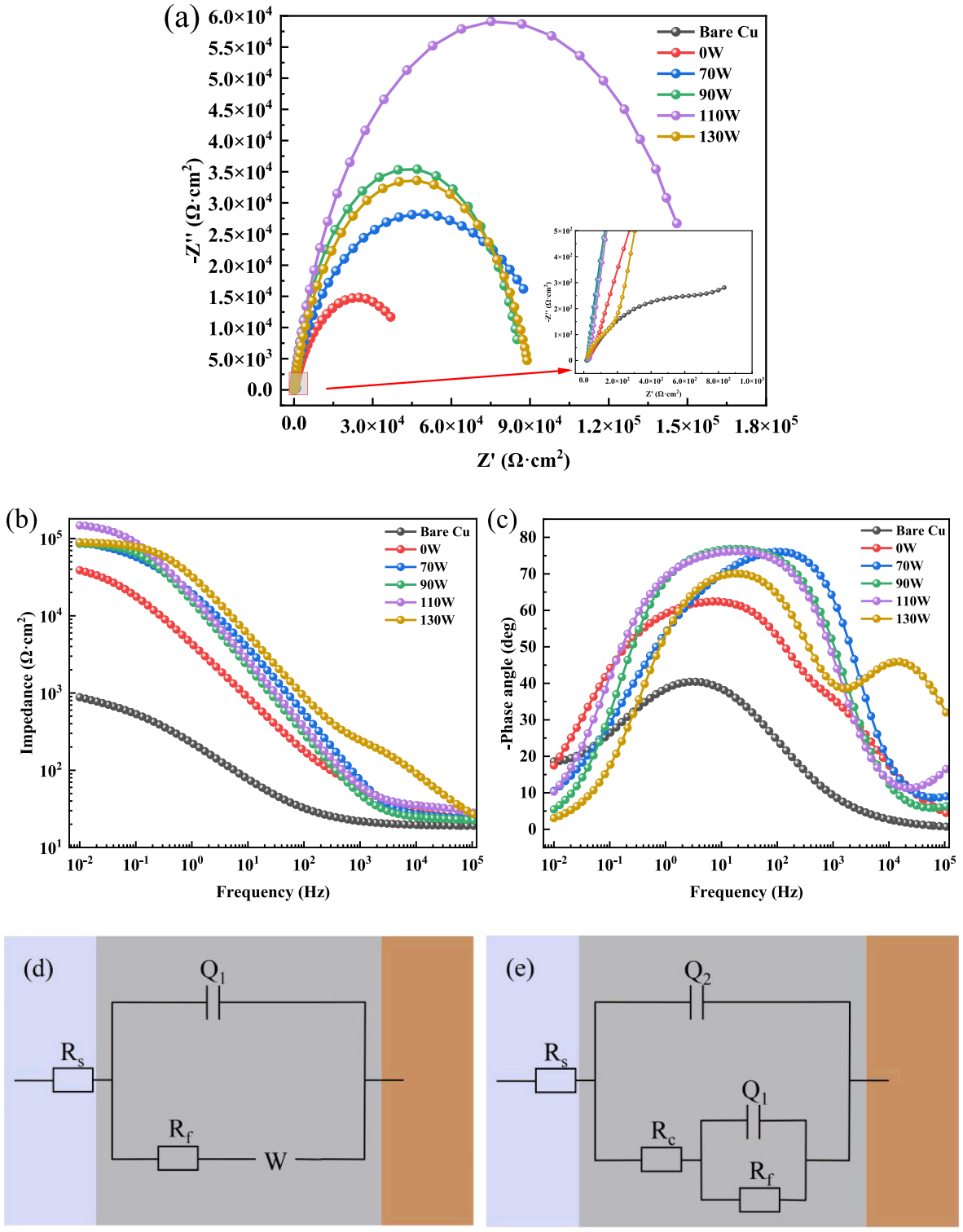

Fig. 6. EIS profiles of different NbTiN coating specimens and bare brass: (a) Nyquist plot, (b) Bode-impedance, (c) Bode-phase angle, (d) and (e) equivalent circuits for bare brass substrate and NbTiN coating, respectively.

maximum value of $1.62 \times 10^5\ \Omega\ cm^2$. A larger charge transfer resistance R_f implies greater diffusion resistance of corrosive ions, resulting in a lower corrosion rate for the coating and a significant improvement in corrosion resistance, which corresponds to the previous analytical results.

3.3. Wettability analysis of the coating

The wettability of coatings on the surface of copper alloys significantly influences their anti-corrosion and anti-fouling properties. Researchers characterize wettability by analyzing the contact angle (CA) formed by water droplets on solid surfaces. The contact angle is mainly influenced by factors such as surface composition, surface morphology, and the surface free energy of the material [61]. When the contact angle

Table 3
Equivalent circuit fitting parameters for different NbTiN-coated specimens and bare brass.

Sample	R_s ($\Omega \cdot cm^2$)	Q_1 ($F \cdot cm^2$)	n_1	R_c ($\Omega \cdot cm^2$)	Q_2 ($F \cdot cm^2$)	n_2	R_f ($\Omega \cdot cm^2$)	Z_w ($\Omega \cdot cm^2$)	χ^2 (10^{-4})
Bare Cu	18.88 ± 0.47	(1.35 ± 0.25) × 10^{-3}	0.58 ± 0.12	–	–	–	(8.56 ± 0.23) × 10^2	0.0154 ± 0.0039	3.48
Nb/(Nb,Ti)N-0W	22.58 ± 1.12	(5.33 ± 0.12) × 10^{-5}	0.68 ± 0.01	222.60 ± 5.10	(7.51 ± 0.48) × 10^{-6}	0.88 ± 0.05	(4.84 ± 0.56) × 10^4	–	1.63
Nb/(Nb,Ti)N-70W	24.11 ± 1.32	(1.04 ± 0.49) × 10^{-5}	0.53 ± 0.03	21.22 ± 4.30	(3.70 ± 0.25) × 10^{-6}	0.94 ± 0.07	(9.05 ± 0.57) × 10^4	–	2.10
Nb/(Nb,Ti)N-90W	21.81 ± 0.47	(4.55 ± 0.32) × 10^{-6}	0.91 ± 0.06	5227 ± 231	(7.68 ± 0.16) × 10^{-6}	0.71 ± 0.07	(1.06 ± 0.03) × 10^5	–	2.16
Nb/(Nb,Ti)N-110W	20.63 ± 0.68	(3.23 ± 0.12) × 10^{-6}	0.61 ± 0.02	36.36 ± 4.86	(8.58 ± 0.61) × 10^{-6}	0.89 ± 0.06	(1.62 ± 0.06) × 10^5	–	1.65
Nb/(Nb,Ti)N-130W	19.77 ± 0.81	(2.90 ± 0.20) × 10^{-6}	0.74 ± 0.01	308.90 ± 13	(2.95 ± 0.39) × 10^{-6}	0.87 ± 0.01	(1.03 ± 0.02) × 10^5	–	1.41

is less than 90°, the material is considered hydrophilic, while a contact angle greater than 90° indicates that the surface is hydrophobic [62]. As illustrated in Fig. 7((a)–(f)), the water contact angles for all samples are presented. The bare brass substrate displays the smallest contact angle, approximately 63.1° ± 1.3°, which indicates typical hydrophilicity. This behavior is mainly attributed to the strong polarization state of the solid, leading to high surface energy, which allows water droplets to have a good affinity for the surface, making them easy to wet and spread. The contact angle of the NbN coating measures 82.8° ± 1.2°, indicating that the pure NbN coating is hydrophilic, consistent with the findings reported by Ren et al. [30]. As the Ti target power increases, the contact angle of the NbTiN coating shows an initial increase followed by a decrease. Notably, at a Ti target power of 110 W, the coating achieves the highest contact angle of about 98.8° ± 1.4°, indicating that doping with Ti (110 W) transforms the wetting state of the NbN coating from hydrophilic to hydrophobic. From the perspective of corrosion resistance, an increased contact angle helps inhibit the erosion of corrosive media, thereby ensuring the stability and durability of the coating. The observed changes in the contact angle are attributed to the combined effects of surface structure and composition. On one thing, Ti doping refines the grain size of the NbN coating, resulting in a denser microstructure that thereby reduces its water affinity. On the other hand, Ti doping modifies the chemical composition of the coating, leading to the formation of TiN and Ti/NbNO phases. These phases further diminish the surface energy of the thin film, significantly mitigating the adsorption strength of water molecules on the coating surface [63].

3.4. Fouling behavior analysis of the coating

The fouling behavior of the coating was evaluated through static suspension testing. The variation in the fouling amount per unit area for both bare brass and NbTiN coating samples immersed in a supersaturated $CaCO_3$ solution at 60 °C over a period of 12 h was analyzed using weighing methods. Theoretically, the mass of $CaCO_3$ accumulates with longer immersion times. Therefore, the weighing measurement was carried out by measuring the mass at different time intervals of 3, 6, 9, and 12 h, so as to analyze the fouling behavior of each sample. The mass of fouling deposition per unit area was determined according to equation (2), and the results are depicted in Fig. 8. During the early stages of immersion (0–6 h), the average $CaCO_3$ fouling rates for the various samples were as follows: bare brass (0.0205 mg/(cm^2·h)), NbN (0 W) (0.0088 mg/(cm^2·h)), NbTiN (70 W) (0.0062 mg/(cm^2·h)), NbTiN (90 W) (0.0062 mg/(cm^2·h)), NbTiN (110 W) (0.0031 mg/(cm^2·h)), and NbTiN (130 W) (0.0060 mg/(cm^2·h)). Among these, the fouling rate for the bare brass substrate was the highest, reaching 6.6 times that of the NbTiN (110 W) coating. In the later stage of immersion (9–12 h), the fouling rates for the samples changed to: bare bass (0.0067 mg/(cm^2·h)), NbN (0 W) (0.0133 mg/(cm^2·h)), NbTiN (70 W) (0.0061 mg/(cm^2·h)), NbTiN (90 W) (0.0052 mg/(cm^2·h)), NbTiN (110 W) (0.0008 mg/(cm^2·h)), and NbTiN (130 W) (0.0058 mg/(cm^2·h)). Notably, the fouling rate for the NbTiN (110 W) coating decreased to 25.8 % of its initial rate, indicating a significant slowdown in fouling adsorption, thus demonstrating the stability and durability of the anti-fouling performance of the NbTiN coating.

Over the entire fouling process (12 h), the most substantial $CaCO_3$ deposition was observed on the bare brass (0.1754 mg/cm^2), followed by the undoped NbN (0 W) coating (0.1627 mg/cm^2). As the Ti target power increased, the fouling masses on the NbTiN coatings exhibited a trend of first decreasing and then increasing, with values of 0.0732 mg/cm^2, 0.0702 mg/cm^2, 0.0387 mg/cm^2, and 0.0718 mg/cm^2. The Nb/

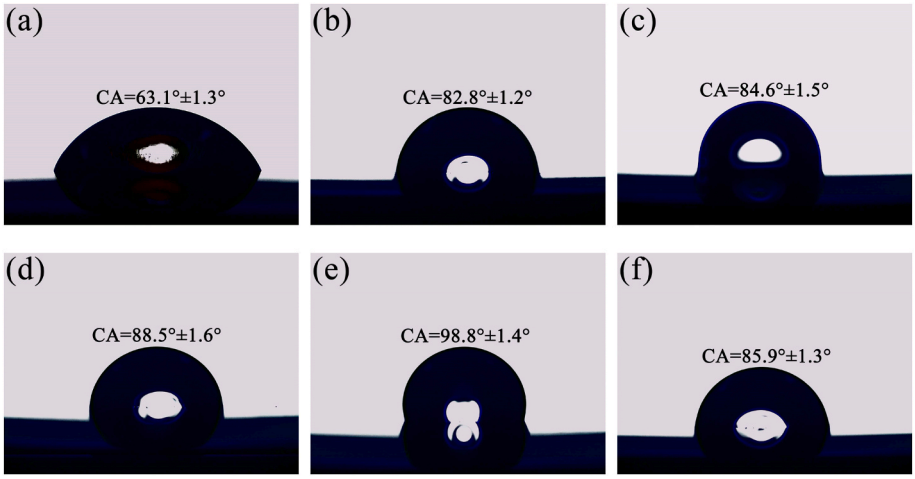

Fig. 7. Water contact angles of samples: (a) bare brass, (b) 0 W, (c) 70 W, (d) 90 W, (e) 110 W, and (f) 130 W.

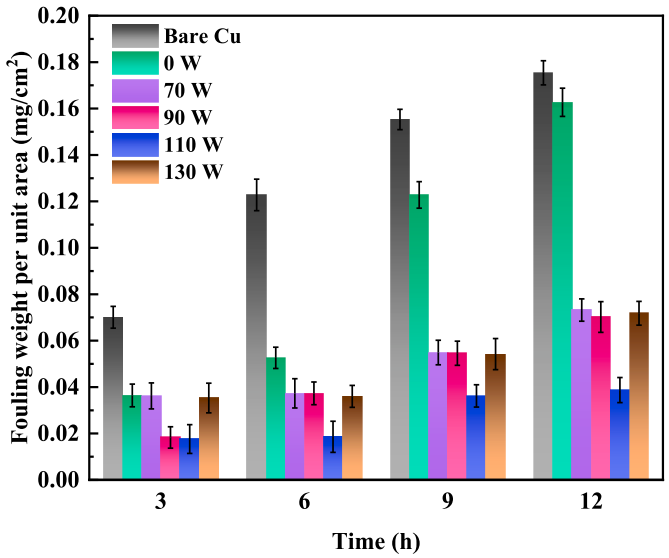

Fig. 8. Variation of $CaCO_3$ fouling with time on bare brass and NbTiN coating surfaces.

(Nb,Ti)N-110 W sample had the lowest $CaCO_3$ fouling amount, representing only 23.8 % of that of the NbN (0 W) coating. When compared to bare brass, the fouling inhibition rates reached 77.94 %. The significant reduction in fouling for the NbTiN (110 W) coating can be attributed to several factors: Ti doping reduces surface defects, resulting in a denser and smoother structure that reduces attachment sites for $CaCO_3$. Moreover, the wetting state of the sample surface transforms to a more hydrophobic condition, decreasing surface energy and inhibiting the adsorption and crystallization of Ca^{2+} ions [21,64]. These findings indicate that Ti doping modifies the NbN coatings in a way that reduces total adsorption and crystalline deposition rates on bare brass substrates in a $CaCO_3$ environment.

The fouling morphologies on the surfaces of bare brass and NbTiN-coated samples, after immersion in a $CaCO_3$ solution for 12 h, were further examined using SEM (Fig. 9(a)–(f)). It was observed that the $CaCO_3$ deposits mainly exhibited cube-shaped, spherical, and needle-like morphologies. According to the literature, these crystal forms of calcium carbonate correspond to calcite, vaterite, and aragonite, respectively [65,66]. A significant number of $CaCO_3$ particles were deposited on the surface of the bare brass substrate (Fig. 9(a)), mainly in the form of massive calcite structures. These structures were uneven in size and shape, highly stable, and difficult to remove from the surface. Some large crystals, formed by the twinning of particles, exceeded 10 μm in size and demonstrated a high packing density and obvious aggregation. This accumulation is attributed to the high surface energy of bare brass, which attracts Ca^{2+} and CO_3^{2-} from the solution, resulting in a faster rate of crystallization and adsorption of $CaCO_3$ on the surface. The extensive fouling increases heat transfer resistance on the copper surface, adversely affecting its thermal conductivity. In the case of the NbN (0 W) coating, the packing density of $CaCO_3$ particles was significantly reduced, and the aggregation phenomenon was weakened. Smaller particles of the deposit tended to form conjugated structures (Fig. 9(b)). This indicates that the presence of the NbN coating affects the formation of $CaCO_3$ by reducing the nucleation and growth of $CaCO_3$ crystals. This is primarily attributed to the alterations in surface structure and composition following the sputtering of the NbN coating, which reduce the surface energy, thereby suppressing the adsorption and crystallization processes of $CaCO_3$. Furthermore, $CaCO_3$ particles on the Ti-doped NbTiN coating surface exhibit a sparser and more isolated distribution, with their size reduced to approximately 2 μm (Fig. 9(c)–(f)). Notably, when the Ti target power was set to 110 W, the number of $CaCO_3$ crystals on the coating surface was significantly reduced, indicating that the NbTiN (110 W) coating effectively inhibits the adsorption and crystalline growth of $CaCO_3$, exhibiting the lowest tendency for fouling. In addition, the ImageJ software was used to analyze the microscopic morphology of scaling on all samples and calculate the proportion of area covered by $CaCO_3$. The results showed that the $CaCO_3$ coverage area ratios of the bare brass, NbN (0 W), NbTiN (70 W), NbTiN (90 W), NbTiN (110 W), and NbTiN (130 W) coated samples were 61.38 %, 27.47 %, 9.36 %, 5.68 %, 3.83 %, and 8.57 % in sequence. This result is consistent with the test result of $CaCO_3$ scaling amount per unit area (Fig. 8).

Fig. 10 presents a diagram of the fouling mechanism for bare brass and NbTiN-coated samples. In Fig. 10(a), the bare brass substrate is affected by both fouling and corrosion within the test environment, resulting in a significant deposition of $CaCO_3$ crystals on its surface. This phenomenon is primarily due to the strong polarization state of the solid, which results in high surface energy. This characteristic increases the adsorption capacity of the bare brass surface for Ca^{2+} and CO_3^{2-} ions, promoting the nucleation and growth of $CaCO_3$ crystals, and ultimately leading to the formation of a stable calcite structure [67]. In addition, the adsorption of Cl^- ions corrodes the surface of the bare brass substrate, causing pitting corrosion, which creates more sites for $CaCO_3$ attachment. In contrast, the undoped samples (Fig. 10(b)) exhibit changes in surface structure and composition that reduce surface energy. For instance, the water contact angle of the NbN (0 W) coating increases from 63.1° to 82.8°, indicating a weakened adsorption strength for water molecules. This reduction inhibits contact between Ca^{2+} and CO_3^{2-} ions. Moreover, previous polarization curve tests indicated a significant decrease in corrosion current density for the NbN coating, from 1.244×10^{-5} A/cm^2 (brass) to 3.679×10^{-7} A/cm^2 (0 W). This inherent chemical inertness of NbN acts as a barrier against Cl^- erosion and inhibits the formation of preferential nucleation sites for $CaCO_3$ crystals. However, the presence of defects such as local pits and pinholes on the NbN coating, along with its typical columnar crystal structure, creates pathways for corrosive media, increasing the risk of galvanic corrosion. Consequently, this can lead to coating failure, exposing the substrate to the coupling effects of corrosion and fouling.

After the introduction of Ti element into the NbN coating, its surface anti-fouling performance was continuously enhanced (Fig. 10(c)). The anti-fouling efficiency of the sample prepared under the 110 W condition reached 77.94 %, with only trace amounts of isolated small-particle fouling present on its surface (Fig. 9(e)). First of all, the incorporation of Ti altered the chemical composition of the coating, introducing TiN and a greater proportion of oxynitride/oxide phases. These phases possess lower surface energy, increasing the water contact angle from 82.8° (0 W) to 98.8° (110 W) and enhancing hydrophobicity. This elevation in hydrophobicity raises the energy barrier for heterogeneous nucleation of fouling on the coating surface, thereby extending the incubation period for scale formation. Secondly, the introduction of Ti promoted the formation of a distinct double-layer structure in the coating, which inhibited the generation of slender pinhole defects and improved the overall compactness of the coating. This enhanced compactness hindered the corrosion of the substrate and coating surface by Cl^- and CO_3^{2-} in corrosive environments. As a result, the corrosion current density decreased by two orders of magnitude relative to the bare brass, reaching as low as 1.148×10^{-7} A/cm^2. The high corrosion resistance prevented ionic corrosion, maintained the smooth and intact morphology of the coating surface, thereby inhibiting the adsorption and crystallization of scale on its surface and reducing the binding energy between scale and the coating. Finally, Ti doping also refined the surface microstructure of the coating, reducing the presence of coarse surface structures and pit defects (Fig. 2). This further increased the adsorption resistance of scale on the coating surface and further enhanced the anti-scaling effect of the coating [68].

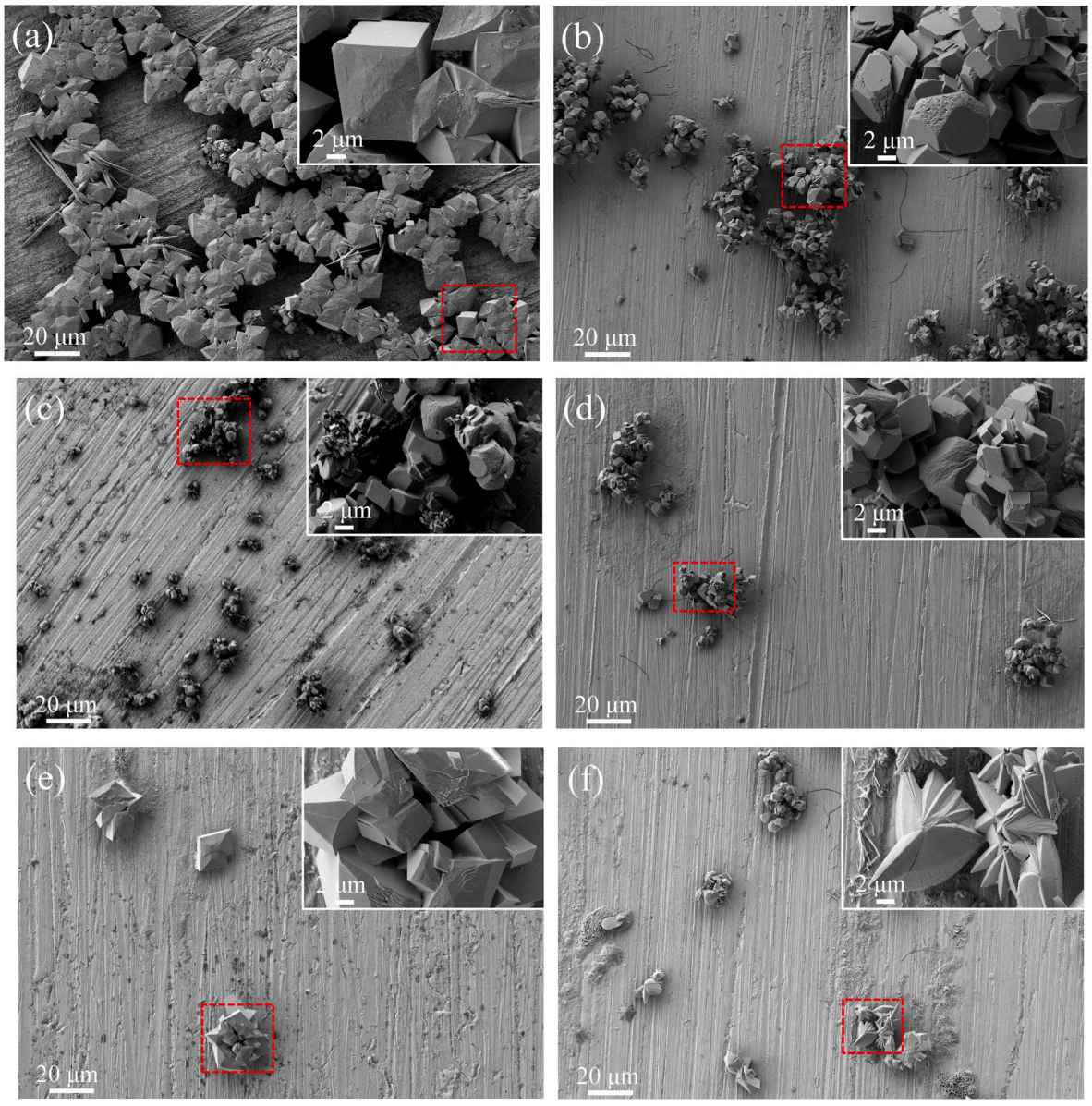

Fig. 9. Microscopic morphology of samples after 12 h of immersion in a supersaturated $CaCO_3$ solution: (a) bare brass, (b) 0 W, (c) 70 W, (d) 90 W, (e) 110 W, and (f) 130 W.

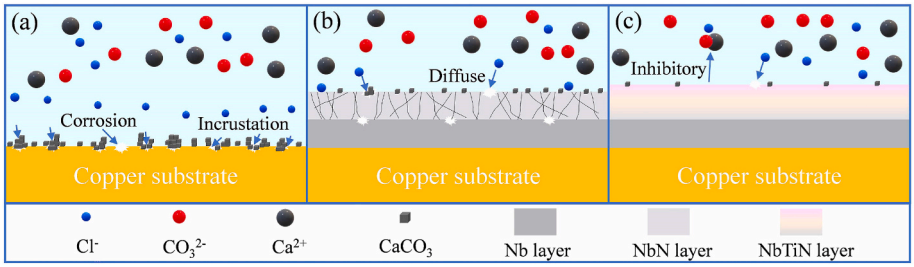

Fig. 10. Schematic diagram of the fouling mechanism: (a) bare brass, (b) undoped sample, and (c) 110 W doped sample.

4. Conclusion

This study examined the impact of Ti target power on the microstructure, corrosion resistance, wettability, and fouling behavior of NbTiN coatings using both RF and DC co-sputtering techniques. The primary conclusions are as follows.

(1) The incorporation of Ti into the NbN coating led to the formation of NbN and TiN composite phases. Ti doping effectively inhibited the development of the columnar crystal structure within the coating, refined the grain size, and established a distinct double-layer structure at the interface. However, excessive Ti doping

(130 W) was found to encourage the sprouting of penetrating columnar crystals and the emergence of pinhole defects.

(2) The NbTiN coating substantially improved the corrosion resistance of the H62 brass substrate. The optimal corrosion resistance of the NbTiN coating was observed at a Ti target power of 110 W, exhibiting a corrosion current density of 1.148×10^{-7} A/cm^2, which is two orders of magnitude lower than that of the bare brass sample (1.244×10^{-5} A/cm^2).

(3) The addition of Ti resulted in grain refinement and a reduction in surface porosity of the NbTiN coating. Moreover, Ti doping reduced the surface energy by changing the chemical bonding state of the coating surface. The NbTiN (110 W) coating displayed the highest water contact angle of $98.8^\circ \pm 1.4^\circ$, indicating superior hydrophobic properties.

(4) The NbTiN coating significantly inhibited the nucleation and adsorption of $CaCO_3$ crystals. As the Ti target power increased, the adsorption of $CaCO_3$ initially decreased and then increased. Notably, the NbTiN (110 W) coating achieved a minimal scale accumulation of 0.0387 mg/cm^2, resulting in a scale inhibition rate of 77.94 % compared to bare brass.

CRediT authorship contribution statement

Wei Li: Writing – review & editing, Software, Data curation. **Can Xiong:** Writing – review & editing, Writing – original draft, Investigation, Data curation, Conceptualization. **Xiulan Li:** Writing – original draft, Investigation, Conceptualization. **Xinjun Zhou:** Methodology, Investigation, Conceptualization. **Yao Chen:** Software, Data curation. **Fei You:** Software, Data curation. **Zhengyu Guo:** Software, Data curation. **Yuan Zhang:** Software, Data curation. **Gui He:** Software, Data curation.

Declaration of competing interest

The authors declare that they have no known competing financial interests or personal relationships that could have appeared to influence the work reported in this paper.

Acknowledgement

This research was financially supported by the Key Research and Development Project of Sichuan Province Science and Technology Department (No. 2023YFG0239), the Graduate Innovation Fund Project of Sichuan University of Science & Engineering (No. Y2024012, Y2024015, Y2024024).

Data availability

Data will be made available on request.

References

[1] X.H. Zeng, P. He, M.L. Hu, W.K. Zhao, H.T. Chen, L.H. Liu, J. Sun, J.L. Yang, Copper inks for printed electronics: a review, Nanoscale 14 (43) (2022) 16003–16032, https://doi.org/10.1039/D2NR03990G.

[2] X.H. Ren, H.Y. Wang, J. Chen, W.L. Xu, Q.Q. He, H.Y. Wang, F.Y. Zhan, S.W. Chen, L.Y. Chen, Emerging 2D copper-based materials for energy storage and conversion: a review and perspective, Small 19 (8) (2023) 2204121, https://doi.org/10.1002/smll.202204121.

[3] H.T.N. Nguyen, N.T. Nguyen, K.L.D. Ngo, H.B. Do, P.P.A. Huy, M.J. Kim, S.V. P. Vattikuti, N.N. Dang, Self-formation of naturally incorporated praseodymium and copper oxide/hydroxide layer on the copper surface in a saline solution, Ceram. Int. 51 (2025) 37398–37411, https://doi.org/10.1016/j.ceramint.2025.05.446.

[4] O.A.G. Noriega, J. Porcayo-Calderon, H. Martinez, R. Lopez-Sesenes, J. G. Gonzalez-Rodriguez, Effect of plasma treatment of copper on its corrosion behaviour in 3.5% NaCl solution, Int. J. Electrochem. Sci. 18 (3) (2023) 100049, https://doi.org/10.1016/j.ijoes.2023.100049.

[5] X.M. She, J. Peng, Y.J. Qiang, Y. Zhou, S. Zhang, Recent advances in protective technologies against copper corrosion, J. Mater. Sci. Technol. 201 (2024) 75–94, https://doi.org/10.1016/j.jmst.2024.02.060.

[6] Y. Luo, Z.L. Chen, W.S. Xu, Z.W. Chen, X.C. Wang, B.Y. Hong, X. Ruan, Study on scale formation and corrosion behavior of heat exchanger steel 20 at different temperatures, Int. J. Electrochem. Sci. 19 (3) (2024) 100510, https://doi.org/10.1016/j.ijoes.2024.100510.

[7] Z.H. Yan, D. Zhou, Q.H. Zhang, Y.T. Zhu, Z.G. Wu, A critical review on fouling influence factors and antifouling coatings for heat exchangers of high-salt industrial wastewater, Desalination 553 (2023) 116504, https://doi.org/10.1016/j.desal.2023.116504.

[8] Z.D. Liu, Y.C. Wang, B. Zhao, X. Jiang, Z.M. Xu, Experimental study on the prevention of microbial fouling accumulation on a Ni-Cu-P modified heat exchange surface, Adv. Powder Technol. 34 (7) (2023) 104023, https://doi.org/10.1016/j.apt.2023.104023.

[9] J. Xu, J.D. Zhao, Y. Jia, Experimental study on the scale inhibition effect of the alternating electromagnetic field on $CaCO_3$ fouling on the heat exchanger surface in different circulating cooling water conditions, Int. J. Therm. Sci. 192 (2023) 108388, https://doi.org/10.1016/j.ijthermalsci.2023.108388.

[10] F. Omidali, S. Azizian, B. Sohrabi, E. Shabanlou, B. Jaleh, Fabrication of highly-hydrophobic steel meshes using pulsed laser ablation and surface modification methods for oil/water separation, Surf. Interfaces 64 (2025) 106402, https://doi.org/10.1016/j.surfin.2025.106402.

[11] J.H. Zhang, X. Cao, A.H. Jiang, L. Ru, S.M. Tao, J.R. Xiao, Corrosion and wear resistance of SiC: Cu: A-C composite films prepared by magnetron sputtering, Surf. Coat. Technol. 464 (2023) 129543, https://doi.org/10.1016/j.surfcoat.2023.129543.

[12] H. Du, J.Y. Wen, G.H. Song, H. Wu, J.A. Feng, Y. Huang, Y.J. Wang, Y.S. Yin, Effect of inserting a-C layers on anticorrosion behavior of Ni-NiCr-NiCrAlSi composite coating on copper through magnetron sputtering for marine applications, Thin Solid Films 808 (2024) 140558, https://doi.org/10.1016/j.tsf.2024.140558.

[13] Z.R. He, C.S. Liu, X.H. Jie, W.Q. Lian, S.T. Luo, Preparation of anti-fouling heat transfer surface by magnetron sputtering a-C film on electrical discharge machining Cu surface, Surf. Coat. Technol. 369 (2019) 44–51, https://doi.org/10.1016/j.surfcoat.2019.03.075.

[14] Y.S. Wang, X. Chen, T.Y. Wu, W. Wei, X.Y. Sui, E.Q. Xie, B. Yang, Z.X. Zhang, Growth and optical properties of erbium-doped gallium nitride thin films prepared by pulsed direct current magnetron sputtering, Appl. Surf. Sci. 716 (2025) 164701, https://doi.org/10.1016/j.apsusc.2025.164701.

[15] X.C. Huang, M. Sun, X. Shi, J.L. Shao, M.H. Jin, W.N. Liu, R.H. Zhang, S.W. Huang, Y.M. Ye, Chemical vapor deposition of transparent superhydrophobic anti-icing coatings with tailored polymer nanoarray architecture, Chem. Eng. J. 454 (2023) 139981, https://doi.org/10.1016/j.cej.2022.139981.

[16] J.B. Liu, Z.F. Chen, P. Chai, Q. Wan, Effects of deposition temperature on microstructure and electrical resistivity of intrinsic CVD-SiC, Ceram. Int. 51 (2025) 24935–24944, https://doi.org/10.1016/j.ceramint.2025.03.174.

[17] N.C. Lee, M. Shin, H. Jung, J. Lee, H. Lee, H. Kim, J. Ahn, J. Bang, H. Song, J. T. Han, J.H. Park, A. Ahmed, M. Ehab, M.U. Munir, Y. Jeong, Copper superfilling of carbon nanotube assembly with long-tortuous pore via one-step electroplating, Surf. Coat. Technol. 505 (2025) 132078, https://doi.org/10.1016/j.surfcoat.2025.132078.

[18] F. Delkhosh, A. Qotbi, A.H. Behroozi, V. Vatanpour, Magnetron sputtering in membrane fabrication and modification: applications in gas and water treatment, J. Ind. Eng. Chem. 143 (2024) 85–108, https://doi.org/10.1016/j.jiec.2024.08.052.

[19] M. Akhtar, S.A. Uzair, M. Rizwan, M.A. Ur Rehman, The improvement in surface properties of metallic implant via magnetron sputtering: recent progress and remaining challenges, Front. Mater. 8 (2022) 747169, https://doi.org/10.3389/fmats.2021.747169.

[20] C.S. Oon, S.N. Kazi, M.A. Hakimin, A.H. Abdelrazek, A.R. Mallah, F.W. Low, S. K. Tiong, I.A. Badruddin, S. Kamanger, Heat transfer and fouling deposition investigation on the titanium coated heat exchanger surface, Powder Technol. 373 (2020) 671–680, https://doi.org/10.1016/j.powtec.2020.07.010.

[21] K. Shaikh, S.N. Kazi, M.N.M. Zubir, B.A. Razak, K. Wong, Y.H. Wong, W.A. Khan, S. Abdullah, M.S. Alam, Investigation of zirconium (Zr) coated heat exchanger surface for the enhancement of heat transfer and retardation of mineral fouling, J. Taiwan Inst. Chem. Eng. 153 (2023) 105246, https://doi.org/10.1016/j.jtice.2023.105246.

[22] Q. Meng, X.Z. Yue, L.L. Shang, X.X. Liu, F. Wang, G.A. Zhang, Corrosion behavior of metallic coatings on titanium bipolar plates of proton exchange membrane water electrolysis, Int. J. Hydrogen Energy 63 (2024) 1105–1115, https://doi.org/10.1016/j.ijhydene.2024.03.242.

[23] H.T. Ye, Z.K. Tu, S. Li, Electrochemical performance of metal nitride coated titanium bipolar plate for proton exchange membrane water electrolyser, J. Power Sources 595 (2024) 234052, https://doi.org/10.1016/j.jpowsour.2024.234052.

[24] Z.B. Qi, Z. Wu, D. Zhang, J. Zuo, Z. Wang, Microstructure, mechanical properties and oxidation behaviors of magnetron sputtered NbN x coatings, J. Alloys Compd. 675 (2016) 22, https://doi.org/10.1016/j.jallcom.2016.03.109.

[25] A. Farhadizadeh, J. Salamania, M.A. Sortica, D. Primetzhofer, M. Oden, Structure evolution during growth of epitaxial NbN films on Al_2O_3 (0006) deposited by magnetron sputtering and its impact on electrical properties, J. Cryst. Growth 656 (2025) 128094, https://doi.org/10.1016/j.jcrysgro.2025.128094.

[26] S. Atta, S. Dash, A.T. Mathew, U.N. Kumar, Recent developments on titanium based mono and multilayer nitride films deposited through HiPIMS, Next Mater. 9 (2025) 100983, https://doi.org/10.1016/j.nxmate.2025.100983.

[27] A.D. Pogrebnjak, V.M. Rogoz, O.V. Bondar, N.K. Erdybaeva, S.V. Plotnikov, Structure and physicomechanical properties of NbN-based protective nanocomposite coatings: a review, Protect. Met. Phys. Chem. Surface 52 (5) (2016) 802–813, https://doi.org/10.1134/S2070205116050191.
[28] Y.I. Chen, Y.X. Gao, L.C. Chang, Y.E. Ke, B.W. Liu, Mechanical properties, bonding characteristics, and oxidation behaviors of Nb–Si–N coatings, Surf. Coat. Technol. 350 (2018) 831–840, https://doi.org/10.1016/j.surfcoat.2018.04.042.
[29] M. Benkahoul, M.K. Zayed, C.S. Sandu, L. Martinu, J.E.K. Sapieha, Structural, tribo-mechanical, and thermal properties of NbAlN coatings with various Al contents deposited by DC reactive magnetron sputtering, Surf. Coat. Technol. 331 (2017) 172–178, https://doi.org/10.1016/j.surfcoat.2017.10.038.
[30] P. Ren, Y.X. Si, G.G. Wang, X.Y. Yang, S.X. Du, Y. Li, J.X. Qiu, S.Z. Zhang, Novel production techniques for solid solution Nb–Y–N films with improved tribological properties and hydrophobic behavior, Vacuum 194 (2021) 110621, https://doi.org/10.1016/j.vacuum.2021.110621.
[31] J. Hao, K. Zhang, P. Ren, J.H. Chen, M.J. Wang, Y. Zhang, M. Wen, Tuning the wettability, mechanical and tribological properties of NbN films by doping rare earth cerium, J. Alloys Compd. 814 (2020) 152339, https://doi.org/10.1016/j.jallcom.2019.152339.
[32] P. Ren, K. Zhang, S.X. Du, Q.N. Meng, X. He, S. Wang, M. Wen, W.T. Zheng, Tailoring the surface chemical bond states of the NbN films by doping Ag: achieving hard hydrophobic surface, Appl. Surf. Sci. 407 (2017) 434–439, https://doi.org/10.1016/j.apsusc.2017.02.199.
[33] R. Franz, M. Lechthaler, C. Polzer, C. Mitterer, Structure, mechanical properties and oxidation behaviour of arc-evaporated NbAlN hard coatings, Surf. Coat. Technol. 204 (2010) 2447, https://doi.org/10.1016/j.surfcoat.2010.01.023.
[34] L. Del Giudice, S. Adjam, D. La Grange, O. Banakh, A. Karimi, R. Sanjinés, NbTiN thin films deposited by hybrid HiPIMS/DC, Surf. Coat. Technol. 295 (2016) 99, https://doi.org/10.1016/j.surfcoat.2015.10.007.
[35] Y.D. Liu, Y. Zou, L. Zhao, W. Liu, L. Cheng, Investigation of adhesion of $CaCO_3$ crystalline fouling on stainless steel surfaces with different roughness, Int. Commun. Heat Mass Tran. 38 (6) (2011) 730–733, https://doi.org/10.1016/j.icheatmasstransfer.2011.04.003.
[36] J.F. Wu, B.B. Wang, J.W. Deng, Z.M. Xu, Q. Zhao, Experimental and mechanism studies on high $CaCO_3$ fouling inhibition of PTFE coating with enhanced stability and anti-corrosion, J. Ind. Eng. Chem. 134 (2024) 65–74, https://doi.org/10.1016/j.jiec.2023.12.037.
[37] L. Jing, J.K. Wu, L.Q. Chang, X.L. Lu, X.P. Li, L. Li, L.J. Ma, J.J. Hao, G.Q. Zhang, Z. F. Deng, J.Z. Yao, D.W. Jing, Effects of DC pulse mode on the performance of nitride coatings: a case study of NbN coatings, Appl. Surf. Sci. 714 (2025) 164398, https://doi.org/10.1016/j.apsusc.2025.164398.
[38] J.Y. Chen, S. Zhang, J. Zheng, Y.F. Dong, C.X. Zhang, J.C. Li, Z.L. Chen, J. Zhang, D. Sun, Excellent anti-corrosion and conductivity of NbN coated on Ti bipolar plate by controlling N_2 flow rates, J. Alloys Compd. 976 (2024) 173033, https://doi.org/10.1016/j.jallcom.2023.173033.
[39] S.S. Lin, Y.L. Gao, S.Y. Hu, S.Y. Fan, Y.S. Tsai, Properties of Ti-doped Al_2O_3 thin films deposited by simultaneous RF and DC magnetron sputtering, Vacuum 107 (2014) 225–230, https://doi.org/10.1016/j.vacuum.2014.02.010.
[40] J.L. Cheng, B. Mi, Q. Wang, H.B. Wang, T. Zhou, Y. Li, H.P. Hou, Y.M. Zhu, Research on magnetron sputtering thin films as electrode materials for supercapacitors, Chem. Eng. J. 509 (2025) 161242, https://doi.org/10.1016/j.cej.2025.161242.
[41] Z.Q. Che, Y. Feng, H. Chen, X.P. Wu, H.Q. Wang, W.P. Yuan, Q.L. Jiang, L. Hou, Y. X. Ou, F.Q. Li, P.A. Zong, HiPIMS-enabled Ti-doped amorphous carbon coatings for high-performance PEMFC bipolar plates, Corros. Sci. 254 (2025) 113053, https://doi.org/10.1016/j.corsci.2025.113053.
[42] M.Y. Ming, D.G. Piliptsou, A.S. Rudenkov, A.V. Rogachev, X.H. Jiang, D.P. Sun, A. S. Chaus, A. Balmakou, Structure, mechanical and tribological properties of Ti-doped amorphous carbon films simultaneously deposited by magnetron sputtering and pulse cathodic arc, Diam. Relat. Mater. 77 (2017) 1–9, https://doi.org/10.1016/j.diamond.2017.05.010.
[43] W. Li, L.T. Liu, Z.X. Li, Y.F. Wang, H.Z. Li, J.J. Lei, Corrosion and conductivity behavior of titanium-doped amorphous carbon film coated SS316L in the environment of PEMFCs, Mater. Chem. Phys. 276 (2022) 125234, https://doi.org/10.1016/j.matchemphys.2021.125234.
[44] Z.X. Yu, X.J. Luo, L.Q. Chang, Y.Y. Ding, J.Z. Yao, Z.F. Deng, C.F. Dong, Enhanced performance of Ti–Nb–N film modified 316L stainless steel and Ti bipolar plates for proton exchange membrane water electrolyser, J. Mater. Res. Technol. 33 (2024) 2478–2488, https://doi.org/10.1016/j.jmrt.2024.09.159.
[45] X.J. Luo, L.Q. Chang, C.H. Ren, Y.Y. Ding, J.H. Zhang, D.W. Zhang, J.Z. Yao, Z. F. Deng, C.F. Dong, Dynamic response to fluctuating input of Nb: Ti: n film modified Ti bipolar plates for proton exchange membrane water electrolyser, Corros. Sci. 249 (2025) 112803, https://doi.org/10.1016/j.corsci.2025.112803.
[46] Y.M. Wu, S.G. Zhou, W.J. Zhao, O.Y. Lu, Comparative corrosion resistance properties between (Cu, Ce)-DLC and Ti co-doped (Cu, Ce)/Ti-DLC films prepared via magnetron sputtering method, Chem. Phys. Lett. 705 (2018) 50–58, https://doi.org/10.1016/j.cplett.2018.05.061.
[47] Y. Ren, J.H. Jia, X.Q. Cao, G.A. Zhang, Q. Ding, Effect of Ag contents on the microstructure and tribological behaviors of NbN–Ag coatings at elevated temperatures, Vacuum 204 (2022) 111330, https://doi.org/10.1016/j.vacuum.2022.111330.
[48] A. Jain, S.P. Ong, G. Hautier, W. Chen, W.D. Richards, S. Dacek, S. Cholia, D. Gunter, D. Skinner, G. Ceder, K.A. Persson, Commentary: the materials project: a materials genome approach to accelerating materials innovation, APL Mater. 1 (1) (2013) 011002, https://doi.org/10.1063/1.4812323.
[49] G.Y. Liu, D.F. Shan, B.Z. Fang, X.D. Wang, Novel hybrid coating of TiN and carbon with improved corrosion resistance for bipolar plates of PEM water electrolysis, Int. J. Hydrogen Energy 48 (50) (2023) 18996–19007, https://doi.org/10.1016/j.ijhydene.2023.02.015.
[50] W. Li, Y. Wang, X.L. Li, X.J. Zhou, X. Jiang, C. Xiong, Y. Chen, F. You, Z.Y. Guo, Y. Zhang, L.T. Liu, X. Li, Effect of Ti doping on properties of TiN/(Ta, Ti) N coated TC4 bipolar plate in proton exchange membrane fuel cells environment, J. Power Sources 631 (2025) 236227, https://doi.org/10.1016/j.jpowsour.2025.236227.
[51] J.E. Alfonso, J. Buitrago, J. Torres, J.F. Marco, B. Santos, Influence of fabrication parameters on crystallization, microstructure, and surface composition of NbN thin films deposited by rf magnetron sputtering, J. Mater. Sci. 45 (2010) 5528–5533, https://doi.org/10.1007/s10853-010-4612-3.
[52] H.B. Ju, N. Ding, J.H. Xu, L.H. Yu, Y.X. Geng, G. Yi, T.Y. Wei, Improvement of tribological properties of niobium nitride films via copper addition, Vacuum 158 (2018) 1–5, https://doi.org/10.1016/j.vacuum.2018.09.037.
[53] Y.L. Wang, S. Li, J. Wang, H.J. Liu, C.L. Zeng, Influence of pulsed-substrate bias duty cycle on microstructure and properties of Nb-doped TiN coatings on PEMFC bipolar plates, J. Mater. Eng. Perform. 3 (2025) 1–10, https://doi.org/10.1007/s11665-025-10905-3.
[54] L. Zhang, C.H. Shang, F.L. Wang, T. Zheng, C.Y. Nie, Y.J. Qiao, G.X. Sun, X. D. Wang, Y.Y. Liu, The wear behavior and corrosion resistance properties of Ni-based composite coatings modified with CeO_2 and MoS_2 nanoparticles, Colloids Surf. 719 (2025) 137017, https://doi.org/10.1016/j.colsurfa.2025.137017.
[55] S. Li, R.M. Jin, S. Li, L.L. Wang, Z.W. Xie, X.G. Li, Z.Q. Wang, High corrosion resistance and conductivity of Al_2O_3/CrN coating for metal bipolar plates in PEMFCs: Al_2O_3 hinders CrN columnar crystals growth, Int. J. Hydrogen Energy 50 (2024) 805–816, https://doi.org/10.1016/j.ijhydene.2023.09.052.
[56] J.M. Zhong, S.H. Zhang, Y. He, Y. Fan, Z.Y. Li, L.P. Yan, H.L. Zhou, X.Y. Cheng, J. X. Song, H.J. Li, Study on the use of furan epoxide modified graphene to enhance the corrosion resistance and wear resistance of electroless Ni-WP coatings, Surf. Coat. Technol. 473 (2023) 129946, https://doi.org/10.1016/j.surfcoat.2023.129946.
[57] J.H. Chu, L.B. Tong, W. Wang, Z.H. Jiang, G.X. Sun, D.N. Zou, K.S. Wang, H. J. Zhang, Sequentially bridged biomimetic graphene-based coating via covalent bonding with an effective anti-corrosion/wear protection for Mg alloy, Colloids Surf. 610 (2021) 125707, https://doi.org/10.1016/j.colsurfa.2020.125707.
[58] S.Y. Wang, Y.J. Shi, T.T. Chen, Q. Wang, Y. Li, K.J. Fan, S.W. Li, Y.S. Liu, Microstructure, wear and corrosion resistance of NiTi coatings synthesized in situ on Ti6Al4V by directed energy deposition with different preheating temperature, J. Alloys Compd. 1026 (2025) 180521, https://doi.org/10.1016/j.jallcom.2025.180521.
[59] S.W. Sun, W.Y. Chen, C.J. Wu, Y. Liu, X.P. Su, J.H. Wang, Effect of calcium on microstructure and corrosion resistance of Zn-6Al-3Mg alloy coatings, Mater. Today Commun. 46 (2025) 112495, https://doi.org/10.1016/j.mtcomm.2025.112495.
[60] Q.D. Wang, S. Kainuma, Y.R. Ju, A. Kim, T. Nishitani, Effect of the spraying process on corrosion resistance and durability of Al-5Mg coating on carbon steel: a comparison of transferred arc plasma spraying and flame spraying methods, Surf. Interfaces 64 (2025) 106377, https://doi.org/10.1016/j.surfin.2025.106377.
[61] L. Ling, S. Cai, Y. Zuo, H.L. Zhang, H. Zhang, M.T. Xue, X.G. Bao, Ultrasound-driven wettability transition of superhydrophobic composite coating modified magnesium alloys with good corrosion resistance and antibacterial properties, Ceram. Int. 50 (15) (2024) 26918–26928, https://doi.org/10.1016/j.ceramint.2024.04.423.
[62] Y.H. Zong, Y. Zhao, W.W. He, Y.H. Jia, H.R. Le, Research on the anti-frost performance of hydrophobic TiN-polymer composite coating on aluminum alloy surface, Compos. Commun. 53 (2025) 102186, https://doi.org/10.1016/j.coco.2024.102186.
[63] J.Y. Han, Y.P. Lan, H.R. Zhang, Z. Xu, K.K. Li, Y.T. Xu, High laser–induced damage threshold, hydrophobicity and optical properties of Nb_2O_5 films post-treated via laser-plasma conditioning and annealing, Ceram. Int. 51 (2025) 39020–39028, https://doi.org/10.1016/j.ceramint.2025.06.142.
[64] C.J. Wang, C.T. Gong, W.X. Sun, W.S. Wang, X.W. Huang, H. Li, Enhanced anti-scaling and anti-corrosion properties of porous superhydrophobic coating with scale inhibitor storage on aluminum alloy substrate, Colloids Surf., A 717 (2025) 136815, https://doi.org/10.1016/j.colsurfa.2025.136815.
[65] J. Jing, L.N. Ren, X.G. Zhang, Y.X. Fu, C.J. Wang, M.L. Li, H.Y. Wang, Z.J. Liu, Robust waterborne superhydrophobic PAI/PTFE/GO@TP anion-release coating with anti-corrosion and anti-scaling performance, Colloids Surf., A 707 (2025) 135836, https://doi.org/10.1016/j.colsurfa.2024.135836.
[66] M.L. Zhu, H.J. Qian, L. Zhang, L.M. Li, C. Wang, J. Kang, C.Y. Lu, Q.H. Gao, Synergistic enhancement of anti-scaling performance in epoxy coatings through surface modification of h-BN and nano-SiO_2, Colloids Surf., A 723 (2025) 137422, https://doi.org/10.1016/j.colsurfa.2025.137422.
[67] M.L. Zhu, H.J. Qian, W.H. Fan, C.J. Wang, R.X. Yuan, Q.H. Gao, H.Y. Wang, Surface lurking and interfacial ion release strategy for fabricating a superhydrophobic coating with scaling inhibition, Pet. Sci. 19 (6) (2022) 3068–3079, https://doi.org/10.1016/j.petsci.2022.07.005.
[68] Z.J. Liu, Y.X. Fu, X.G. Zhang, J.Y. Yang, M.L. Li, L.F. Zhu, S. Guan, H.Y. Wang, Construction of durable superhydrophobic/superoleophilic polyurea–based composite coating with excellent anti–corrosion/scaling properties, Prog. Org. Coating 192 (2024) 108520, https://doi.org/10.1016/j.porgcoat.2024.108520.